Resolving γ-ray overlap of ^{117m}Sn, ^{117}Sb, and ^{123m}Te for cross-section measurement

Zolbadral Tsoodol [a*], **Masayuki Aikawa** [b,c,d], **Hiromitsu Haba** [e], **Ganzul Tsengel** [a], **Battsooj Nankhir** [a]

[a] *Nuclear Research Center, National University of Mongolia, Ulaanbaatar 13330, Mongolia*

[b] *Faculty of Science, Hokkaido University, Sapporo 060-0810, Japan*

[c] *Global Center for Biomedical Science and Engineering, Faculty of Medicine, Hokkaido University, Sapporo 060-8648, Japan*

[d] *Graduate School of Biomedical Science and Engineering, Hokkaido University, Sapporo 060-8638, Japan*

[e] *Nishina Center for Accelerator-Based Science, RIKEN, Wako 351-0198, Japan*

The production cross-sections of ^{117m}Sn, ^{117}Sb, and ^{123m}Te in α-particle induced reactions on ^{nat}Sn were measured up to 50 MeV using the stacked-foil activation technique. A significant analytical challenge arose from the overlapped peak near the 159 keV γ-rays from these nuclides. This overlapped peak was resolved using a time-differential analysis that leveraged the different half-lives (^{117}Sb: 2.8 h, ^{117m}Sn: 13.6 d, ^{123m}Te: 119.2 d). Through γ-ray spectrometry at multiple cooling times (0.6 h to 144.9 d), a sequential subtraction method based on the activation formula was used to distinguish the overlapped peak. The resulting independent cross-sections of these ^{117m}Sn, ^{117}Sb, and ^{123m}Te isotopes, are in good agreement with literature data, thereby validating the method for resolving complex γ-ray interferences.

Key words: Cross section, excitation function, ^{117m}Sn, ^{117}Sb, ^{123m}Te, Talys code.

I. INTRODUCTION

Knowledge of nuclear reaction cross-sections is of primary importance for both fundamental nuclear physics, such as understanding level densities and reaction mechanisms, and a wide range of nuclear applications, including radioisotope production for medicine, waste management, and material science. The production of novel medical radioisotopes for diagnostic and therapeutic purposes continues to be an active and important field of research.

The quantification of production cross-sections using the stacked foil activation analysis depends on measuring characteristic γ-rays. This method becomes significantly challenging when different reaction products emit γ-rays of same or similar energies. Without proper separation of this peak overlap, the results derived will be inaccurate. In our recent experiment of the ^{nat}Sn+α reactions [1], we faced an overlapped peak. This overlapped peak arose from three different radionuclides ^{117g}Sb ($T_{1/2}$ = 2.8 h), ^{117m}Sn ($T_{1/2}$ = 13.6 d), and ^{123m}Te ($T_{1/2}$ = 119.2 d), which were produced simultaneously. Each of these nuclides emits nearly identical energy γ-rays (^{117g}Sb: 158.56 keV, ^{117m}Sn: 158.56 keV, and ^{123m}Te: 159.0 keV), making them indistinguishable.

Since we cannot separate this overlapped peak using the standard γ-ray spectrometry, we use a technique based on measurements of different cooling times. By taking measurements at different cooling times, we can take advantage of the fact that each nuclide decays at a very different rate. This allows us to separate their individual signals from one another.

In our recent natSn+α study targeting ^{118}Te production [1], standard spectrometry could not resolve the composite 159 keV peak arising from the co-produced impurities ^{117}Sb, ^{117m}Sn, and ^{123m}Te. By using their distinct half-lives through time-differential measurements, we successfully separated these signals. This work provides the detailed methodology excluded from our previous report and is essential for determining independent production cross-sections and assessing the radionuclidic purity of this production route.

* Email:ts_zolbadral@num.edu.mn

II. EXPERIMENTAL DETAILS

High-purity metallic foils of natural tin (Sn) and natural titanium (Ti) were used. The ^{nat}Sn foils served as the primary target material, while the Ti foils were used as beam monitors via the well-characterized ^{nat}Ti(α,x)^{51}Cr reaction. The foils were arranged in a stacked-foil configuration to allow for the measurement of the excitation function over a range of energies in a single irradiation.

The target stack was irradiated for 30 minutes at the RIKEN AVF cyclotron with an α-particle beam of initial energy of 51.0 ± 0.2 MeV, determined by the time-of-flight method. The beam current was monitored throughout the irradiation using a Faraday cup and found to be stable, with an average intensity of 201 nA. The energy degradation through the stack was calculated using the SRIM code. A schematic of the irradiation setup is presented in Appendix B.1.

The data for all possible reaction channels contributing to the production of ^{123m}Te, ^{117m}Sn, and ^{117}Sb are summarized in Table 1.

Measurements of the activities of the irradiated foils started approximately 0.6 hours after the end of bombardment (EOB). A high-purity germanium detector (ORTEC GEM30P4-70) coupled with Gamma Studio software (Seiko EG&G) was used for γ-ray spectrometry. The detector efficiency was calibrated using a standard multi-nuclide point source. Detailed cooling and acquisition times were used to separate the overlapped peak into their individual components.

The experiment focused on a specific signal, a "composite 159 keV peak," which is essentially a combination of peaks from multiple sources that are very close and difficult to distinguish individually. To separate the contributions, γ-ray measurements were taken at different "cooling times," which is the period after EOB. The information of the γ-ray measurements is listed in Table 2:

Because of the different half-lives of the isotopes of interest, the ratio of the contributions to the overlapped peak in each series was changed. By waiting for specific periods, some of the isotopes with shorter half-lives had significantly decayed, meaning they no longer contributed to the 159 keV peak. This waiting period systematically reduced the number of overlapped signals in each subsequent measurement, making it easier to analyze the remaining components.

III. DERIVATION OF CROSS SECTIONS

The core of the analysis is a sequential subtraction method designed to separate the counts from each contributing nuclide to the unresolved ~159 keV peak. The method is based on the fundamental activation cross-section formula. The reaction cross-section (σ_r) is related to the measured net counts (N_γ) in a characteristic γ-ray peak by the equation:

$$\sigma_r = \frac{N_\gamma \lambda}{n_T I_p \varepsilon_d \varepsilon_\gamma \varepsilon_t (1-e^{-\lambda t_{irr}}) e^{-\lambda t_c} (1-e^{-\lambda t_m})} \quad (1)$$

where λ is the decay constant, ε_d is detector efficiency, ε_γ is the γ-ray intensity, ε_t is the dead time correction, n_T is the areal number density of the target nucleus, I_p is the beam flux, and t_{irr}, t_c, and t_m are the irradiation, cooling, and measurement times, respectively.

A. Step-1: Separation of ^{123m}Te.

The long-lived metastable state of ^{123}Te ($T_{1/2}$ = 119.2 d) can be directly produced through the reactions listed in Table 1. The analysis began with the last measurement in Table 2, series-7 (S7), taken 145 days after EOB. At this point, after more than 10 half-lives of ^{117m}Sn ($T_{1/2}$ = 13.6 d), the contributions from both ^{117}Sb ($T_{1/2}$ = 2.8 h) and ^{117m}Sn were negligible. The 159 keV peak was therefore purely from the decay of ^{123m}Te.

$$N_{159(S7)}^{^{123m}\mathrm{Te}} = N_{159(S7)}^{\mathrm{total}} \quad (2)$$

The cross-section σ(^{123m}Te) was calculated directly via Eqs. (1) and (2).

Table 1: Reactions and decay data for the investigated reaction products [2–4]. *γ lines in bold were used in our evaluation.*

Nuclide	Half-life	Decay mode (%)	E_γ (keV)	I_γ (%)	Contributing reaction	Q-value (MeV)	Threshold energy (MeV)
^{123m}Te	119.2 d	ε+β^+(100)	**159.0**	**84.3(3)**	^{119}Sn(α,γ)	1.28	0
					^{120}Sn(α,n)	-7.82	8.09
					^{122}Sn(α,3n)	-22.85	23.64
					^{124}Sn(α,5n)	-37.25	38.54
^{117}Sb	2.8 h	ε (100)	**158.562**	**85.9**	^{114}Sn(α,p)	-6.78	6.97
					^{115}Sn(α,d)	-12.11	12.44
					^{116}Sn(α,t)	-15.41	15.83
					^{117}Sn(α,nt)	-22.35	22.95
					^{118}Sn(α,2nt)	-31.67	32.52
					^{119}Sn(α,3nt)	-38.16	39.16
					^{120}Sn(α,4nt)	-47.27	48.49
					From ^{117}Te		
^{117m}Sn	14.00 d	IT (100)	156.02	2.113(12)	^{115}Sn(α,2p)	-12.10	12.53
			158.56	**86.4(4)**	^{116}Sn(α,^{3}He)	-13.94	14.43
					^{117}Sn(α,pt)	-20.12	20.83
					^{118}Sn(α,nα)	-9.64	9.98
					^{119}Sn(α,2nα)	15.50	16.67

Table 2: γ-ray measurement information (cooling time, measurement distance, and dead time in each series).

Series	Measurement	Series	Measurement
S_1	0.6–2.4 h, 5–100 cm, 0.3–1.9 %	S_5	1.8–2.9 d, 5–20 cm, 0.2–1.0 %
S_2	2.5–5.7 h, 5–75 cm, 0.2–1.7 %	S_6	10.3–12.2 d, 5–10 cm, 0.2–1.0 %
S_3	5.9–10.9 h, 5–50 cm, 0.1–1.6 %	S_7	144–145 d, 5 cm, <0.1 %
S_4	20.9–33.2 h, 5–20 cm, 0.1–1.4 %		

B. Step 2: Separation of ^{117m}Sn

^{117m}Sn ($T_{1/2}$ = 14 d) can be directly produced through several nuclear reactions listed in Table 1. The analysis proceeded to series-6 (S6), taken 10.3–12.2 days after EOB. At this cooling time, ^{117}Sb had completely decayed, but the peak had contributions from ^{117m}Sn and ^{123m}Te. The net counts from ^{117m}Sn were separated by subtracting the predicted contribution of ^{123m}Te:

$$N_{159(S6)}^{^{117m}\mathrm{Sn}} = N_{159(S6)}^{\mathrm{total}} - N_{159(S6)}^{^{123m}\mathrm{Te}} \quad (3)$$

Further details are provided in Appendix A.1.

The term $N_{159(S6)}^{^{123m}\mathrm{Te}}$ was calculated using Eq. (3) with the known σ(^{123m}Te) from Step 1 and the specific experimental parameters (t_c, t_m, ε_t) of the S6 measurement. The resulting separated counts, $N_{159(S6)}^{^{117m}\mathrm{Sn}}$, were then used in Eq. (1) to determine the cross-section σ(^{117m}Sn).

C. Step 3: Separation of ^{117}Sb

Finally, the analysis was applied to the earliest measurement, series-1 (S1), taken 0.6–2.4 hours after EOB. The spectra were the most complex, containing contributions from all three isotopes. The counts from ^{117}Sb were separated by subtracting the predicted contributions from both longer-lived nuclides:

$$N_{159(S1)}^{^{117}\mathrm{Sb}} = N_{159(S1)}^{\mathrm{total}} - N_{159(S1)}^{^{123m}\mathrm{Te}} - N_{159(S1)}^{^{117m}\mathrm{Sn}} \quad (4)$$

Additional details can be found in Appendix A.2.

The two subtracted terms were calculated using Eqs. (1-3) with their respective known cross-sections σ(^{123m}Te) from Step 1 and σ(^{117m}Sn) from Step 2 and the experimental parameters of the S1 measurement. The residual counts were qualified only to ^{117}Sb and were used to calculate its cross-section, σ(^{117}Sb).

IV. RESULTS AND DISCUSSION

The analysis above was successfully applied to the γ-ray spectra from each foil in the stack, allowing for the determination of the energy-dependent production cross-sections.

A. Determination of ^{123m}Te

The excitation function of the ^{nat}Sn(α,x)^{123m}Te reaction, derived from series-7 (S7) measurement, is shown in Fig. 1 in comparison with previously published experimental data [5] and theoretical calculations [6].

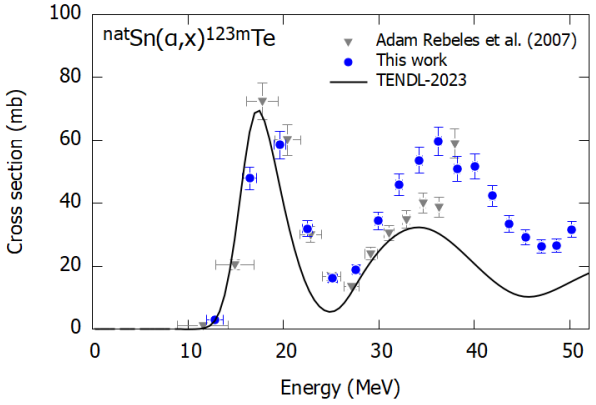

Fig. 1. Excitation function of the ^{nat}Sn(α,x)^{123m}Te reaction.

Our results are in good agreement with the previous experimental data reported by Adam Rebeles et al. (2007), validating the overall shape and magnitude of the cross-section, which is characterized by two distinct peaks. Our data provide the clearer second peak structure between 30 and 40 MeV.

The TENDL-2023 prediction, however, shows significant deviations. While it correctly identifies the position of the first peak near 18 MeV. More critically, the theoretical model fails to reproduce the second broad peak centered around 36 MeV, underestimating its cross-section by approximately a factor of two. This discrepancy indicates that the theoretical models used in the TENDL-2023 evaluation describe inadequately the reaction mechanisms responsible for the second peak, suggesting a need for model modification at higher energies.

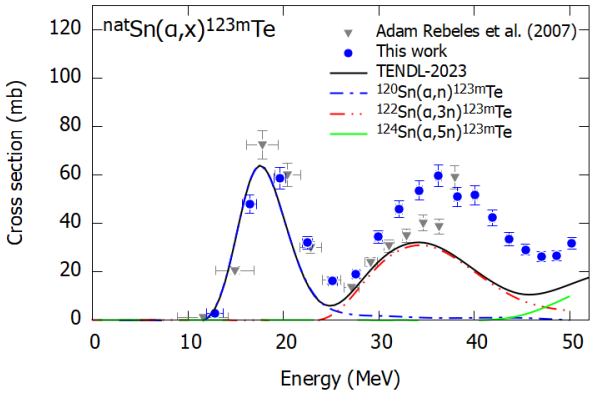

Fig. 2. Measured excitation function of the ^{nat}Sn(α,x)^{123m}Te reaction in comparison with Talys (default) calculation.

We show our experimental results for the ^{nat}Sn(α,x)^{123m}Te reaction with calculations from the TALYS-2.0 code (default parameters) [7] in Fig. 2. The default parameters accurately describe the low-energy region dominated by the ^{120}Sn(α,n)^{123m}Te reaction, but they significantly underestimate the high-energy region dominated by ^{122}Sn(α,3n)^{123m}Te.

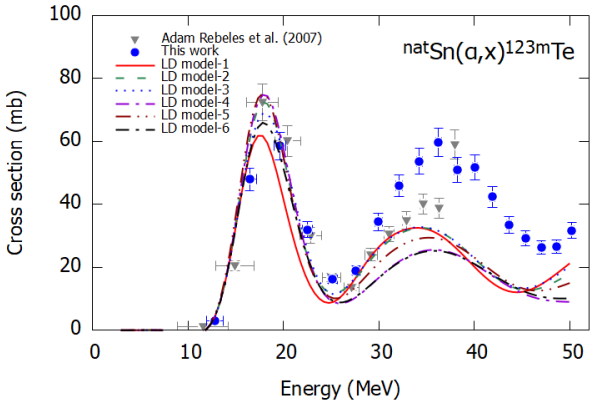

Fig. 3. Measured excitation function of the ^{nat}Sn(α,x)^{123m}Te reaction in comparison with Talys level density models.

Additionally, we tested all six level density (LD) models available in the TALYS code [7] and compared the results with experimental data sets as shown in Fig.3. The comparison reveals that the

phenomenological models (LD Models 1, 2, and 3) generally provide a better description of the experimental data than the microscopic models (LD Models 4, 5, and 6). Specifically, the other models yield better agreement for the first peak ^{120}Sn(α,n)^{123m}Te than LD Model-1 (Constant Temperature + Fermi Gas) predicting a lower cross-section maximum. For the second peak of the ^{122}Sn(α,x)^{123m}Te reaction, all models underestimate the experimental maximum of approximately 60 mb. The LD Models 1–3 predict higher cross-sections of about 32 mb, whereas the microscopic models yield values around 25 mb. Although the peak magnitude is systematically underestimated, the LD Models more accurately reproduce the overall shape of the excitation function.

To investigate the physical origin of the discrepancy observed in the 30-40 MeV region, we performed a comprehensive sensitivity analysis on the Optical Model Potential (OMP) parameters beyond the volume radius modification. Following the standard OMP parameterization in TALYS, we systematically adjusted the surface imaginary potential depth (W_d) and the surface diffuseness (a_d) using the wdadjust and adadjust keywords, respectively. However, our analysis revealed that the calculated cross-sections in this specific energy region are largely insensitive to variations in these surface parameters within physically reasonable limits (±30%). The calculation showed significant sensitivity solely to the geometry of the real volume potential (r_v). Consequently, the 1.4-fold increase in the radius presented in Fig. 2 is not intended to suggest a physical expansion of the nucleus, but rather to demonstrate that the standard global optical model potentials currently available in TALYS fail to reproduce the reaction mechanism for this specific channel without extreme geometric modifications. This suggests a need for a more rigorous revision of the microscopic pre-equilibrium models or level densities for this mass region, rather than simple adjustments to surface absorption parameters.

B. Determination of ^{117m}Sb

The term evaluated using Eq. (3) with the known σ(^{123m}Te) from Step 1 and the specific experimental parameters (t_c, t_m, ε_t) of the S6 measurement. The resulting separated counts, $N_{159(S6)}^{^{117m}\mathrm{Sn}}$, are then used in Eq. (1) to determine the cross-section σ (^{117m}Sn).

Figure 4 shows the excitation function for the ^{nat}Sn(α,x)^{117m}Sn reaction, determined from the S6 measurement, together with previous experimental data [5] and theoretical calculations [6].

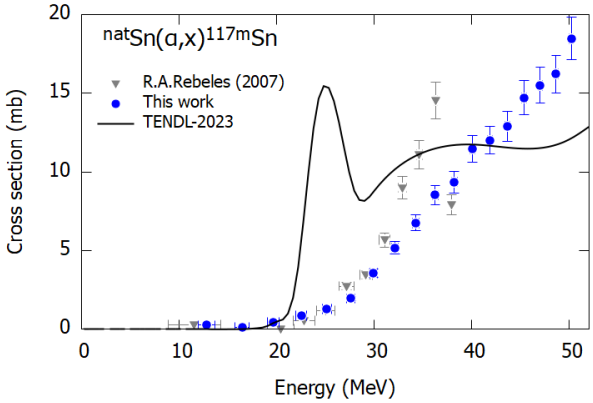

Fig. 4. Excitation function of the ^{nat}Sn(α,x)^{117m}Sn reaction.

Present results generally show good agreement with previously published experimental data for natural tin [5], particularly concerning the trend and magnitude of the cross-section below 30 MeV.

Both experimental datasets show an overall increasing trend in the reaction cross-section from the threshold energy up to 50 MeV. While in the 30–40 MeV region, the data reported by Adam Rebeles et al. (2007) show larger scatter, including a local decrease around 38 MeV, and a data point near 35 MeV that lies above the trend established by the present work. The observed scatter in the experimental data can be attributed to the varying contributions of the individual reaction channels to the ^{nat}Sn(α,x)^{117m}Sn reaction, as shown in Fig. 5.

However, the surrounding data points are in better agreement, and most of our data points are consistent with the earlier measurements within their respective experimental uncertainties. This overall consistency aids in confirming our separation method and showing the accuracy of the measured values for this reaction channel. In contrast, a notable discrepancy is observed with respect to the TENDL-2023 theoretical model, particularly in the prediction of a sharp resonance. This suggests that the nuclear model parameters and reaction mechanisms employed in the TENDL evaluation for this reaction channel may require

significant revision in order to accurately reproduce the experimental results.

To investigate the origin of this discrepancy, we analyzed the individual reaction channels contributing to the total cross-section. Figure 5 presents the theoretical decomposition of the ^{nat}Sn(α,x)^{117m}Sn reaction based on the TENDL-2023 evaluation. The production of ^{117m}Sn involves contributions from ^{117}Sn(α,α)^{117m}Sn, ^{118}Sn(α,αn)^{117m}Sn, ^{119}Sn(α,α2n)^{117m}Sn and ^{120}Sn(α,α3n)^{117m}Sn reactions.

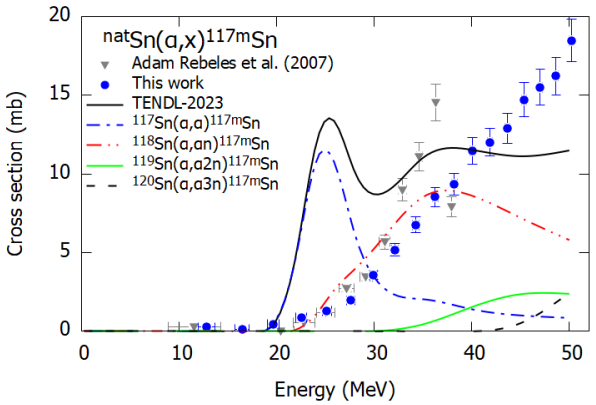

Fig. 5. Measured excitation function of the ^{nat}Sn(α,x)^{117m}Sn reaction in comparison with Talys calculations.

As clearly shown in Fig. 5, the sharp peak predicted around 25 MeV is dominated entirely by the ^{117}Sn(α,α)^{117m}Sn inelastic scattering channel. The calculation predicts a substantial cross-section for this channel that is absent in the experimental data, suggesting that the theoretical model significantly overestimates the probability of inelastic scattering populating the isomeric state at these energies.

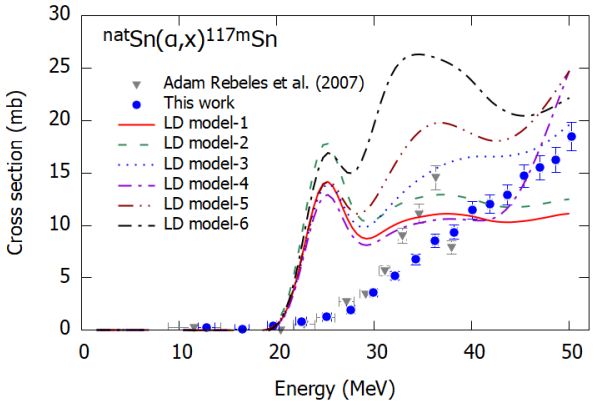

Fig. 6. Measured excitation function of the ^{nat}Sn(α,x)^{117m}Sn reaction in comparison with Talys level density models.

Furthermore, we performed calculations using the six different level density models available in the TALYS code [7] to see if the issue could be resolved by adjustments. As shown in Fig. 6, the sharp resonance peak near 25 MeV is consistently observed across all six models, whereas the experimental data exhibits a smooth, monotonic rise. This confirms that the peak is not an artifact of the level density parameterization but rather stems from the optical model inputs or the description of the inelastic scattering mechanism for the ^{117}Sn isotope. Regarding the high-energy region (>35 MeV), the microscopic models (LD Models 4, 5, and 6) significantly overestimate the magnitude, while the phenomenological models (LD Models 1, 2, and 3) provide a closer approximation to the experimental values, though they still fail to reproduce the correct shape of the excitation function.

C. Determination of ^{117}Sb

In addition to the direct reaction channels detailed in Table 1, ^{117}Sb ($T_{1/2}$ = 2.8 h) is also formed indirectly via the complete decays of co-produced ^{117g}Te ($T_{1/2}$ = 62 min, $\varepsilon+\beta^+$: 100%) and ^{117m}Te ($T_{1/2}$ = 103.0 ms, IT: 100%). Consequently, the measured cross sections presented for the ^{nat}Sn(α,x)^{117}Sb reaction are cumulative values. The cumulative cross sections of ^{117}Sb, $\sigma_d^{(cum)}$, can be determined using $N_{159}^{^{117}Sb}$ that also includes the contribution from ^{117g}Te and ^{117m}Te. We use the cumulative production cross sections of ^{117g}Te and the equation in Appendix A.3 to obtain the independent cross sections σ(^{117}Sb).

The resulting excitation function is shown in Fig. 7, in comparison with the previously measured cross sections on natural tin [5] and the theoretical predictions from TENDL-2023 [6].

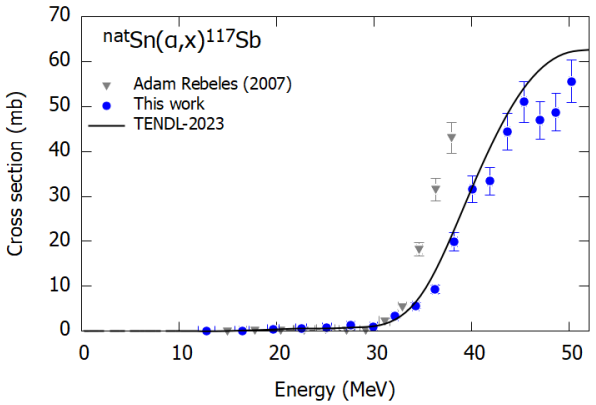

Fig. 7. Excitation function of the $^{nat}Sn(\alpha,x)^{117}Sb$ reaction.

Present results are in good agreement with the TENDL-2023 evaluation across the entire measured energy range. The theoretical curve accurately reproduces the reaction threshold, the sharp rise, and the magnitude of the measured cross-sections.

A comparison with the previous experimental data reported by Adam Rebeles et al. (2007) shows some notable discrepancies. While there is general agreement at lower energies, the data points reported by Adam Rebeles et al. (2007) between 33 and 38 MeV are systematically and significantly higher than our measurements.

V. SUMMARY

The independent production cross-sections for radionuclides produced by the irradiation of natural tin with α-particles up to 50 MeV were measured. A severe interference caused by the overlap of γ-rays from ^{117m}Sn, ^{117}Sb, and ^{123m}Te at 159 keV was resolved using a time-differential analysis. The observed cooling time dependence was eliminated by applying a sequential subtraction method. This method allowed for the successful distinguish of the overlapped γ-ray peak and the determination of the independent production cross-sections for each of the three interfering nuclides. The overall consistency of the results with existing literature and theoretical models validates the presented method.

ACKNOWLEDGEMENTS

The experiment was carried out at RI Beam Factory operated by RIKEN Nishina Center and CNS, University of Tokyo, Japan. The authors would like to thank A. Nambu, Y. Shigekawa, Y. Kanayama, H. Shimizu, and S. Mitra of RIKEN Nishina Center for their technical assistance with the experiment. This research was partially performed by the commissioned research fund provided by F-REI (JPFR24040201 and JPFR25040201).

REFERENCES

[1] Z. Tsoodol, M. Aikawa, L. Bold, D. Gantumur, A. Nambu, S. Ebata, and H. Haba, Alpha-particle-induced reactions on natural tin for production of 118Te, Applied Radiation and Isotopes 225, 112053 (2025).

[2] International Atomic Energy Agency, *LiveChart of Nuclides.*, https://www-nds.iaea.org/livechart/.

[3] National Nuclear Data Center, *Nuclear Structure and Decay Data On-Line Library, Nudat 2.8*, http://www.nndc.bnl.gov/nudat2/.

[4] B. Pritychenko and A. Sonzogni, *Q-Value Calculator (QCalc)*, http://www.nndc.bnl.gov/qcalc/.

[5] R. Adam Rebeles, A. Hermanne, S. Takács, F. Tárkányi, S. F. Kovalev, and A. Ignatyuk, Alpha induced reactions on natSn: An experimental study of excitation functions and possible production pathways, Nucl Instrum Methods Phys Res B 260, 672 (2007).

[6] A. J. Koning, D. Rochman, J. C. Sublet, N. Dzysiuk, M. Fleming, and S. van der Marck, TENDL: Complete Nuclear Data Library for Innovative Nuclear Science and Technology, Nuclear Data Sheets 155, 1 (2019).

[7] A. Koning, S. Hilaire, and S. Goriely, TALYS-2.0 Simulation of Nuclear Reactions (User Manual), 2023.

APPENDIX A.1

$$N_{159(S6)}^{^{117m}\mathrm{Sn}} = N_{159(S6)}^{\mathrm{total}} - \sigma_{(S7)}^{^{123m}\mathrm{Te}} \left(\frac{n_T I_b \varepsilon_{d(S6)} I_{159}^{^{123m}\mathrm{Te}} \varepsilon_{t(S6)} \left(1 - e^{-\lambda_{^{123m}\mathrm{Te}} T_b}\right) e^{-\lambda_{^{123m}\mathrm{Te}} T_{c(S6)}} \left(1 - e^{-\lambda_{^{123m}\mathrm{Te}} T_{m(S6)}}\right)}{\lambda_{^{123m}\mathrm{Te}}} \right) =$$

$$= N_{159(S6)}^{\mathrm{total}} - \frac{N_{159(S7)}^{^{123m}\mathrm{Te}} \lambda_{^{123m}\mathrm{Te}}}{n_T I_b \varepsilon_{d(S7)} I_{159}^{^{123m}\mathrm{Te}} \varepsilon_{t(S7)} \left(1 - e^{-\lambda_{^{123m}\mathrm{Te}} T_b}\right) e^{-\lambda_{^{123m}\mathrm{Te}} T_{c(S7)}} \left(1 - e^{-\lambda_{^{123m}\mathrm{Te}} T_{m(S7)}}\right)}$$

$$\times \left(\frac{n_T I_b \varepsilon_{d(S6)} I_{159}^{^{123m}\mathrm{Te}} \varepsilon_{t(S6)} \left(1 - e^{-\lambda_{^{123m}\mathrm{Te}} T_b}\right) e^{-\lambda_{^{123m}\mathrm{Te}} T_{c(S6)}} \left(1 - e^{-\lambda_{^{123m}\mathrm{Te}} T_{m(S6)}}\right)}{\lambda_{^{123m}\mathrm{Te}}} \right)$$

$$= N_{159(S6)}^{\mathrm{total}} - N_{159(S7)}^{^{123m}\mathrm{Te}} \left(\frac{\varepsilon_{d(S6)} \varepsilon_{t(S6)} e^{-\lambda_{^{123m}\mathrm{Te}} T_{c(S6)}} \left(1 - e^{-\lambda_{^{123m}\mathrm{Te}} T_{m(S6)}}\right)}{\varepsilon_{d(S7)} \varepsilon_{t(S7)} e^{-\lambda_{^{123m}\mathrm{Te}} T_{c(S7)}} \left(1 - e^{-\lambda_{^{123m}\mathrm{Te}} T_{m(S7)}}\right)} \right)$$

APPENDIX A.2

$$N_{159(S1)}^{^{117}\mathrm{Sb}} = N_{159(S1)}^{\mathrm{total}} - N_{159(S7)}^{^{123m}\mathrm{Te}} \left(\frac{\varepsilon_{d(S1)} \varepsilon_{t(S1)} e^{-\lambda_{^{123m}\mathrm{Te}} T_{c(S1)}} \left(1 - e^{-\lambda_{^{123m}\mathrm{Te}} T_{m(S1)}}\right)}{\varepsilon_{d(S7)} \varepsilon_{t(S7)} e^{-\lambda_{^{123m}\mathrm{Te}} T_{c(S7)}} \left(1 - e^{-\lambda_{^{123m}\mathrm{Te}} T_{m(S7)}}\right)} \right)$$

$$- N_{159(S6)}^{^{117m}\mathrm{Sn}} \left(\frac{\varepsilon_{d(S1)} \varepsilon_{t(S1)} e^{-\lambda_{^{117m}\mathrm{Sn}} T_{c(S1)}} \left(1 - e^{-\lambda_{^{117m}\mathrm{Sn}} T_{m(S1)}}\right)}{\varepsilon_{d(S6)} \varepsilon_{t(S6)} e^{-\lambda_{^{117m}\mathrm{Sn}} T_{c(S6)}} \left(1 - e^{-\lambda_{^{117m}\mathrm{Sn}} T_{m(S6)}}\right)} \right)$$

APPENDIX A.3

The cumulative cross sections of ^{117}Sb, $\sigma_d^{(cum)}$, can be determined using $N_{159}^{^{117}\mathrm{Sb}}$ that also includes the contribution from the decay of ^{117g}Te. We use the production cross sections of ^{117g}Te and the cumulative equation to obtain the independent cross sections $\sigma^{^{117}\mathrm{Sb}}$.

$$\sigma^{^{117}\mathrm{Sb}} = \sigma_d^{(cum)} - \varepsilon_p \sigma_p \frac{\lambda_p}{(\lambda_d - \lambda_p)} \left\{ \frac{\lambda_d \lambda_d}{\lambda_p \lambda_p} \frac{\left(1 - e^{-\lambda_p T_b}\right) e^{-\lambda_p T_c} \left(1 - e^{-\lambda_p T_m}\right)}{\left(1 - e^{-\lambda_d T_b}\right) e^{-\lambda_d T_c} \left(1 - e^{-\lambda_d T_m}\right)} - 1 \right\}$$

where p (parent) and d (daughter) mean ^{117g}Te and ^{117}Sb, respectively.

APPENDIX A.4

According to error propagation, the uncertainty of $\boldsymbol{N^{123m_{Te}}_{159(S7)}}$ can be defined as

$$\Delta N^{123m_{Te}}_{159(S7)} = \sqrt{N^{total}_{159(S7)} + B}$$

The uncertainty of $N^{117m_{Sn}}_{159(S6)}$ is

$$\Delta N^{117m_{Sn}}_{159(S6)} = \sqrt{\left(\Delta N^{total}_{159(S6)}\right)^2 + \left(\Delta N^{123m_{Te}}_{159(S6)}\right)^2}$$

here

$$\Delta N^{123m_{Te}}_{159(S6)} = N^{123m_{Te}}_{159(S6)} \cdot \sqrt{\left(\frac{\Delta N^{123mTe}_{159(S7)}}{N^{123m_{Te}}_{159(S7)}}\right)^2 + \left(\frac{\Delta \epsilon_d}{\epsilon_d}\right)^2 + (\Delta\text{Time factors})^2}$$

The uncertainty of $N^{117\text{Sb}}_{159(S1)}$ is

$$\Delta N^{117Sb}_{159(S1)} = \sqrt{\left(\Delta N^{total}_{159(S1)}\right)^2 + \left(\Delta N^{123m_{Te}}_{159(S1)}\right)^2 + \left(\Delta N^{117m_{Sn}}_{159(S1)}\right)^2}$$

APPENDIX B.1

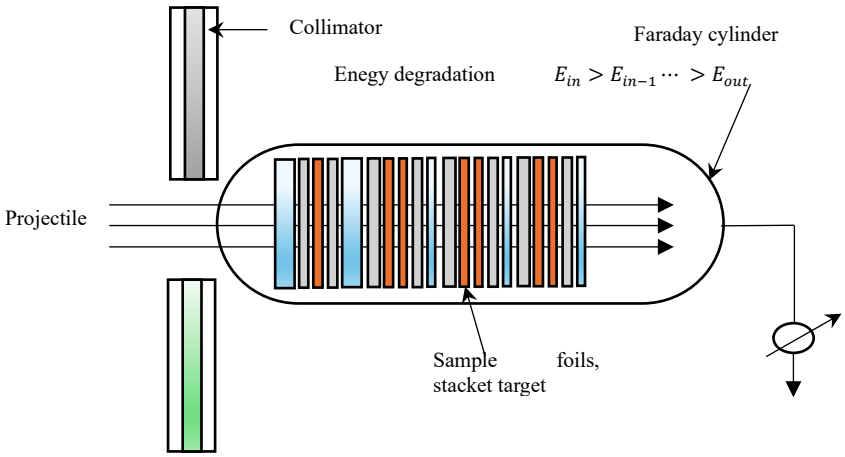

Fig. 8. Schematic representation of the stacked-foil irradiation setup, showing the collimator, alternating sample/monitor foils, and the Faraday cup for beam current monitoring

The incident α-particle beam was shaped by a collimator before striking the target assembly. The target consisted of alternating high-purity Sn sample foils and Ti monitor foils arranged in a stacked-foil configuration. This arrangement allows for the simultaneous measurement of excitation functions over a broad energy range, as the beam energy degrades while passing through the successive foils in the stack. The total beam current and integrated charge were monitored using a Faraday cup (Faraday cylinder) located at the rear of the assembly to ensure accurate flux determination.